Turbulent convection in liquid metal with and without rotation

Eric M. King[a,b,1] and Jonathan M. Aurnou[c]

[a]Department of Physics and [b]Department of Earth and Planetary Science, University of California, Berkeley, CA 94720; and [c]Department of Earth and Space Sciences, University of California, Los Angeles, CA 90095

Edited by Peter L. Olson, Johns Hopkins University, Baltimore, MD, and approved March 8, 2013 (received for review October 8, 2012)

The magnetic fields of Earth and other planets are generated by turbulent, rotating convection in liquid metal. Liquid metals are peculiar in that they diffuse heat more readily than momentum, quantified by their small Prandtl numbers, $Pr \ll 1$. Most analog models of planetary dynamos, however, use moderate *Pr* fluids, and the systematic influence of reducing *Pr* is not well understood. We perform rotating Rayleigh–Bénard convection experiments in the liquid metal gallium ($Pr = 0.025$) over a range of nondimensional buoyancy forcing (*Ra*) and rotation periods (*E*). Our primary diagnostic is the efficiency of convective heat transfer (*Nu*). In general, we find that the convective behavior of liquid metal differs substantially from that of moderate *Pr* fluids, such as water. In particular, a transition between rotationally constrained and weakly rotating turbulent states is identified, and this transition differs substantially from that observed in moderate *Pr* fluids. This difference, we hypothesize, may explain the different classes of magnetic fields observed on the Gas and Ice Giant planets, whose dynamo regions consist of $Pr < 1$ and $Pr > 1$ fluids, respectively.

The interiors of Earth and other terrestrial bodies, as well as the Gas Giant planets, contain vast oceans of flowing metals. Mixed by turbulent convection as these planets cool, the flowing conductors produce electric currents that maintain planetary magnetic fields. These bodies also rotate, and it is expected that the resulting Coriolis forces strongly influence convective dynamo processes. Beyond linear theory (1), however, not much is known about the dynamics of rotating convection in liquid metal that underlie planetary magnetic field generation.

Theory and experiments often focus on a simplified analog of geophysical and astrophysical systems, Rayleigh–Bénard convection (RBC). The RBC system consists of a fluid layer contained between flat, horizontal plates separated by distance h, the bottom of which is warmer than the top by ΔT, and with downward pointing gravity, $\mathbf{g}$. Near the bottom boundary, the fluid warms and expands by a volumetric factor α (per degree kelvin) and similarly cools and contracts near the top boundary, such that the fluid is unstably stratified.

Rotating convection is explored by spinning the RBC system about a vertical axis at an angular rate Ω, which is adopted as the reference frame for the model. The fluid dynamics of the system are characterized by three dimensionless parameters. The Prandtl number, $Pr \equiv \nu/\kappa$, defines the diffusive transport properties of the fluid, where ν and κ are its viscous and thermal diffusivities. The Rayleigh number, $Ra \equiv \alpha g \Delta T h^3/(\nu\kappa)$, prescribes the magnitude of the buoyancy force. Finally, the rotation period is specified by the Ekman number, $E \equiv \nu/(2\Omega h^2)$. The primary diagnostic used in many convection studies, including this one, is the Nusselt number, which characterizes the efficiency of heat transport by convection as $Nu \equiv qh/(k\Delta T)$, where q is total heat flux and k is the fluid's thermal conductivity. Heat flux q is total heat power $\mathcal{P}$ divided by the horizontal surface area of the fluid layer, A.

Rotating convection studies have, to date, focused primarily on moderate Pr fluids. Of recent interest in these studies have been transitions between rotationally dominated and nonrotating turbulent states (2–10) and the enhancement of heat transport by rotation (6, 8, 11–15). Numerical simulations of planetary dynamo action by rotating convection also concentrate on fluids with unit order Pr (16). Scaling analysis of heat transfer in such simulations agrees quantitatively with rotating convection experiments in water (17). Although it is often assumed that planetary cores can be modeled as $Pr = \mathrm{O}(1)$ fluids (e.g., ref. 18), it remains to be seen whether such systematic behavior applies to liquid metal convection.

Liquid metals are special in that, due to electrical conduction, they transport heat more efficiently than momentum, $Pr \lesssim 0.1$. Similarly, the plasmas that constitute stellar convection zones, due to ionic transport, also have $Pr \lesssim 0.1$ (19). For comparable Ra, convection in low Prandtl number fluids is expected to be different from the more conventional $Pr \gtrsim 1$ case in that inertia effects are enhanced for small Pr (e.g., refs. 20–22). All else being equal, nonrotating convection experiments and simulations find that low Pr fluids produce more vigorous convection, yet lower Nu values than moderate Pr fluids (23, 24). Just as varying Pr affects the dynamics of turbulent convection, so too does the influence of rotation. Coriolis forces tend to suppress and constrain convection (1). The stabilizing rotational constraint is overcome in low and moderate Pr fluids by different means. In low Pr fluids ($Pr < 0.67$), convective instability occurs as oscillatory convection, whereby the rotational constraint is overcome by the growth of inertial modes, whereas moderate Pr convection is manifest as stationary rolls in which the rotational constraint is overcome by viscous effects (1). Few studies, however, have ventured far beyond onset to investigate fully turbulent convection in rotating liquid metals.

The most comprehensive rotating liquid metal convection survey is that of Rossby (25), using mercury, whose accessed parameter range is shown in Fig. 1. Nakagawa (26) and Aurnou and Olson (27) also investigate rotating RBC in mercury and gallium, but their studies are limited to convection near onset. Several experiments have been performed using liquid metals in spinning spherical containers, in which convection occurs in response to centrifugal acceleration (28–30). These studies, although important for understanding global convection dynamics in planetary cores, may not be well controlled thermally (31).

Heat Transfer Regimes

We perform Rayleigh–Bénard convection experiments, using the liquid metal gallium with and without rotation. Nonrotating experiments provide a baseline for comparison with rotating experiments. Convection in liquid metal without rotation produces Nu–Ra scaling laws that differ from those of moderate Pr fluids. Convection in moderate Pr fluids often approximately follows the classical heat transfer scaling (32),

$$Nu \sim Ra^{1/3}, \qquad [1]$$

which is attributed to the marginal stability of the thermal boundary layer (33). Low Pr fluids such as liquid metals are more

Author contributions: E.M.K. and J.M.A. designed research; E.M.K. and J.M.A. performed research; E.M.K. analyzed data; and E.M.K. and J.M.A. wrote the paper.

The authors declare no conflict of interest.

This article is a PNAS Direct Submission.

[1]To whom correspondence should be addressed. E-mail: ericmking@gmail.com.

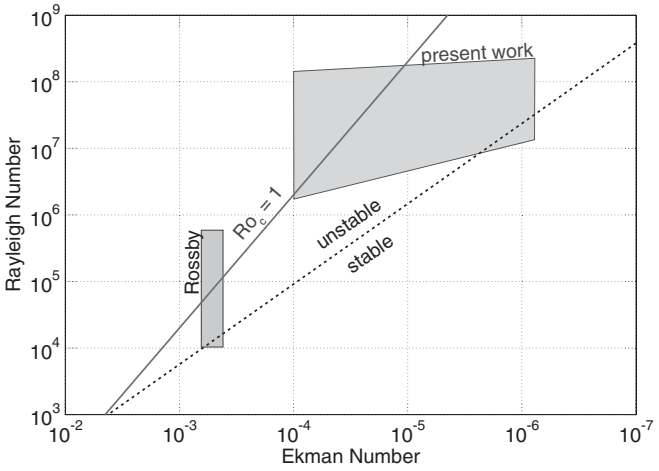

Fig. 1. Experimental parameter space for rotating RBC in liquid metal. Areas accessed by Rossby (25) (using mercury) and this work (gallium) are marked and labeled. The dotted line indicates the predicted onset of oscillatory convection for $Pr = 0.025$ (1). The solid line indicates where $Ro_c = 1$ for $Pr = 0.025$, above which convection is weakly influenced by rotation (Fig. 5).

susceptible to interior turbulence, and inertial effects in the fluid bulk have been shown to take precedence over boundary layer physics in heat transfer processes (34). An inertial heat transfer scaling can be derived (e.g., ref. 35) through two balances: a momentum balance between buoyancy and inertia and a thermal balance between advection in the bulk fluid and diffusion in the boundary layer,

$$U^2/h = \alpha \Delta T g \qquad [2]$$

and

$$U\Delta T/h = \kappa \Delta T/\delta_T^2, \qquad [3]$$

respectively. Here, U is a typical flow speed and δ_T is the thermal boundary layer thickness. The Nusselt number is usually taken to scale with the thermal boundary layer thickness as $Nu = h/(2\delta_T)$, such that Eqs. **2** and **3** predict

$$Nu = \frac{1}{2}(RaPr)^{1/4}. \qquad [4]$$

Similar scaling laws have been observed in previous nonrotating liquid metal convection studies (e.g., refs. 23, 25, 36). Essentially, the difference between scaling laws [**1**] and [**4**] is that in the former the thermal boundary layer thickness is determined by its own marginal stability, whereas in the latter the thermal boundary layer thickness is set by the strength of interior turbulence.

Rotation suppresses convection, such that the onset of convection is delayed, $Ra_c \propto E^{-4/3}$, where Ra_c is the critical Rayleigh number, and, in many cases, less heat is transported by rotating convection than by nonrotating convection. King et al. argue that the heat transfer by rotating RBC with $Pr \geq 1$ is determined by the marginal stability of the boundary layer, which gives a heat transfer scaling law $Nu = (Ra/Ra_c)^3$ (37). Julien et al. analyze an asymptotically reduced system of equations for rapidly rotating RBC, finding the emergence of an "ultimate" regime where $Nu \propto (Ra/Ra_c)^{3/2}$ (38). In this ultimate regime, the primary bottleneck for heat transfer is the rotationally constrained interior turbulence, not thermal boundary layers. Experiments and direct numerical simulations with $Pr \geq 1$ support the marginal boundary layer stability law (7, 37), but simulations of the reduced equations for $Pr \geq 1$ produce scalings similar to the predicted ultimate regime (10, 38). The propensity for strong interior turbulence in low Pr convection suggests that experiments in liquid metals may access this ultimate regime more easily than those using moderate Pr fluids.

Important in the understanding of rotating convection is the transition between rotationally dominated and weakly rotating turbulent states (2–9). For moderate Pr fluids, King et al. use the framework of a marginally stable thermal boundary layer to predict that the transition between the two states occurs at a transitional Rayleigh number (37),

$$Ra_t = E^{-3/2}. \qquad [5]$$

When $Ra_c < Ra < Ra_t$, the boundary layer is stabilized predominantly by the influence of the Coriolis force, and its marginal stability leads to the $Nu = (Ra/Ra_c)^3$ heat transfer scaling law. When $Ra > Ra_t$, the boundary layer is instead stabilized predominantly by rotationally independent diffusive effects, leading to convective heat transfer that is not influenced by rotation ([**1**]). Analysis of rotating convection experiments in water supports the predicted transition scaling: When $Ra < Ra_t$, heat transfer is suppressed relative to nonrotating values; and when $Ra > Ra_t$, Nu values are observed to conform to the nonrotating behavior. This regime transition criterion does not depend on the mechanical boundary conditions, but, when Ekman boundary layers are present, it corresponds to the crossing of the Ekman and thermal boundary layers identified in ref. 3. And, although by different means, a similar regime transition scaling is produced by the analysis of Julien et al. (38).

In liquid metal convection we may expect that the interior turbulence takes precedence over boundary layer physics. In that case, it is generally expected that the transition between rotationally constrained and unconstrained states occurs when the free-fall scaling (2) is in balance with the Coriolis force, leading to a triple balance,

$$U^2/h = \alpha \Delta T g = 2\Omega U, \qquad [6]$$

and, eliminating U, a transitional Rayleigh number,

$$Ra_t \sim E^{-2} Pr. \qquad [7]$$

Thus, the regime transition for low Pr is predicted to occur when the convective Rossby number, $Ro_c \equiv Ra^{1/2} E Pr^{-1/2} = \mathcal{O}(1)$ (e.g., ref. 39).

Methods

A gallium-filled, 20-cm diameter, 20-cm tall right cylinder is heated from below by an electrical resistance element. The fluid is contained by a 0.3-cm thick stainless steel sidewall and by copper top and bottom endwalls with thicknesses 4 and 1.5 cm, respectively. The contact surfaces of the endwalls are coated with thin layers of tungsten to prevent corrosion by the liquid metal without appreciably inhibiting thermal coupling. Between 50 and 4,500 W of heat power $\mathcal{P}$ is produced by the heating element, which is mechanically fixed underneath the bottom endwall, below which is a 10-cm-thick Marinite structural insulator. The convection tank sidewall is insulated by an inner layer of about 20 cm of Insulfrax fibrous, high-temperature thermal blanketing, outside of which is another 10 cm of closed-cell foam insulation. Heat passed through the fluid is removed by a thermostated recirculating bath above the top endwall. Temperature measurements are made near the top and bottom fluid surfaces by two arrays of six thermistors in each endwall, 2 mm from the fluid. Eight more thermistors penetrate the convection tank to characterize the temporal statistics of the flow. The convection tank and diagnostics systems are rotated up to 40 times per minute by a brushless servomotor. Further details on the experimental apparatus are given in refs. 9 and 40.

One hundred eight experiments are conducted with a range of fluid temperatures (at midlevel) between 38 °C and 110 °C and an ensemble median fluid temperature of 44 °C. The thermo-physical properties of liquid gallium are temperature dependent, and so this range must be accounted

for in the calculations of *Pr*, *Ra*, *E*, and *Nu*. Density is typically taken to vary linearly with temperature,

$$\rho = \rho_{mp}\left(1 - \alpha\left(T_{fluid} - T_{mp}\right)\right), \quad [8]$$

where $\rho_{mp} = 6,090$ kg/m^3 is the density of liquid gallium at its melting point, $T_{mp} = 29.8$ °C, and $\alpha = 9.85 \times 10^{-5}$ K^{-1} (41). The temperature dependence of viscosity for liquid metals can be described by

$$\nu = \frac{\eta_0}{\rho} exp(E/RT_{ab}), \quad [9]$$

where $\eta_0 = 4.36 \times 10^{-4}$ Pa·s and $E = 4,000$ J/mol are constants specific to liquid gallium, $R = 8.3144$ J/(K·mol) is the gas constant, and T_{ab} is the absolute temperature of the fluid in kelvins (41). The temperature dependence of the thermal conductivity of liquid gallium is, unfortunately, not very well constrained (42, 43). For simplicity, we elect to use a single value of k such that $Nu = 1$ for our experiment with no convection (see Figs. 3 and 4*A*),

$$k = 32\text{W/mK}, \quad [10]$$

which is within the constraints of several experimental measurements made in our temperature range (e.g., ref. 44). Thermal diffusivity is then calculated as

$$\kappa = k/(\rho c_P), \quad [11]$$

where $c_P = 397.6$ J/kgK is the specific heat of liquid gallium (41).

Given these fluid properties and experimental temperature range, the Prandtl number of our liquid gallium spans the range $0.019 \lesssim Pr \lesssim 0.025$, with a median value of 0.025. Rayleigh numbers accessed in this study range from $2 \times 10^6 \lesssim Ra \lesssim 2 \times 10^8$, and rotating experiments have Ekman numbers $9 \times 10^{-7} \lesssim E \lesssim 10^{-4}$. This parameter range is shown in Fig. 1 and is compared against the most extensive previous study of rotating RBC in liquid metal (25).

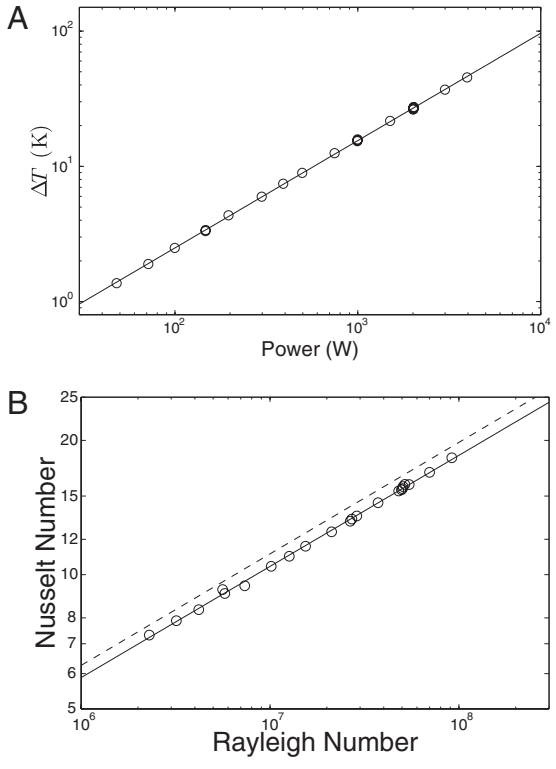

Fig. 2. Heat transfer by nonrotating convection. (*A*) Temperature drop across the layer, ΔT, is plotted vs. the input heat power, $\mathcal{P}$. The solid line shows the best-fitting power law $\Delta T = 0.0652\mathcal{P}^{0.792}$. (*B*) Dimensionless heat transport, *Nu*, is plotted vs. the buoyancy forcing, *Ra*. The solid line shows the best-fit power law $Nu = 0.19Ra^{0.249}$. The dashed line shows the inertial scaling [**4**], $Nu = \frac{1}{2}(RaPr)^{1/4}$, which overestimates measured convective heat flux by 7% on average.

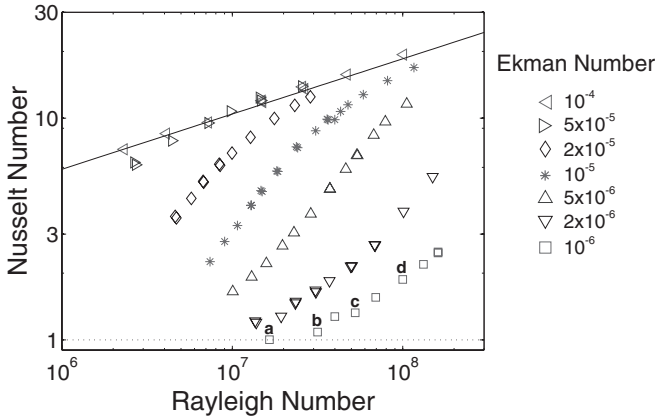

Fig. 3. The Nusselt number is plotted vs. the Rayleigh number for all rotating convection cases. Ekman numbers are indicated by symbol shape (color on line) and generally decrease from top left to bottom right. The lower, dotted line indicates $Nu = 1$. The solid line shows the best-fit nonrotating scaling law, $Nu = 0.19Ra^{0.249}$. Temperature time series from the cases marked **a**–**d** are shown in Fig. 4.

The degree of turbulence is usually quantified by Reynolds numbers, $Re \equiv Uh/\nu$, where U is rms flow speed, and flows with $Re > \mathcal{O}(10^3)$ are typically considered turbulent (45). Although we do not measure flow speeds directly, rough estimates of *Re* can be made using scaling laws. Several different scaling laws, both theoretical (23, 46) and empirical (47), provide similar estimates for maximum rms flow speeds in the present experiments, $Re \approx 2 \times 10^4$. Thus, we expect many of the experiments presented here to be fully developed turbulent convection.

Results

Fig. 2*A* shows measurements of ΔT plotted vs. input heat power, $\mathcal{P}$, for nonrotating convection experiments. A best-fit power law regression yields $\Delta T = 0.0652 \pm 0.002\mathcal{P}^{0.792 \pm 0.004}$ (K/W), which is shown as the solid line in Fig. 2*A*. For three $\mathcal{P}$ values, the mean temperature of the fluid was varied (by changing the top boundary temperature) to quantify heat losses, which should be roughly proportional to the temperature drop between the experiment and the room, $\Delta T_{amb} = T_{fluid} - T_{room}$. For $\mathcal{P} = 2,010$ W, for example, T_{fluid} is varied in six separate experiments from 49 °C to 90 °C. We find that the measured ΔT across the fluid decreases by less than 4% across this range, despite an increase in ΔT_{amb} of 86%. From this we conclude that our heat loss errors are small, and error bars, which would be smaller than the symbol size, are excluded.

Fig. 2*B* shows *Nu* plotted vs. *Ra* for nonrotating convection. A best-fit power law regression to the data yields $Nu = 0.19 \pm 0.01Ra^{0.249 \pm 0.004}$ and is shown as the solid line in Fig. 2*B*. The dashed line in Fig. 2*B* shows the inertial scaling law [**4**] for the median experimental value of $Pr = 0.025$. Experimental heat transfer data trend with this scaling law, but are 7% less than predicted on average.

Fig. 3 shows Nusselt number measurements plotted vs. *Ra* for the rotating experiments. In general, heat transfer by rotating convection is suppressed relative to that for nonrotating convection, which is depicted by the solid line. One case, with $E = 10^{-6}$ and $Ra = 1.6 \times 10^7$, and demarked "**a**," is convectively stable. A time series temperature measurement made within the fluid during that particular experiment is shown in Fig. 4*A*. The onset of convection for $E = 10^{-6}$ is observed to occur between $1.6 \times 10^7 < Ra < 3 \times 10^7$. Linear theory predicts (1) the onset of convective instability at $Ra = 2.4 \times 10^7$ for $E = 10^{-6}$ and $Pr = 0.025$. Our most weakly supercritical experiment, labeled case "**b**" in Fig. 3, convects heat by oscillatory motions in the outer half of the cylinder, $s > 0.5h$, where s is cylindrical radius (48). Fig. 4*B* shows a temperature time series from this case

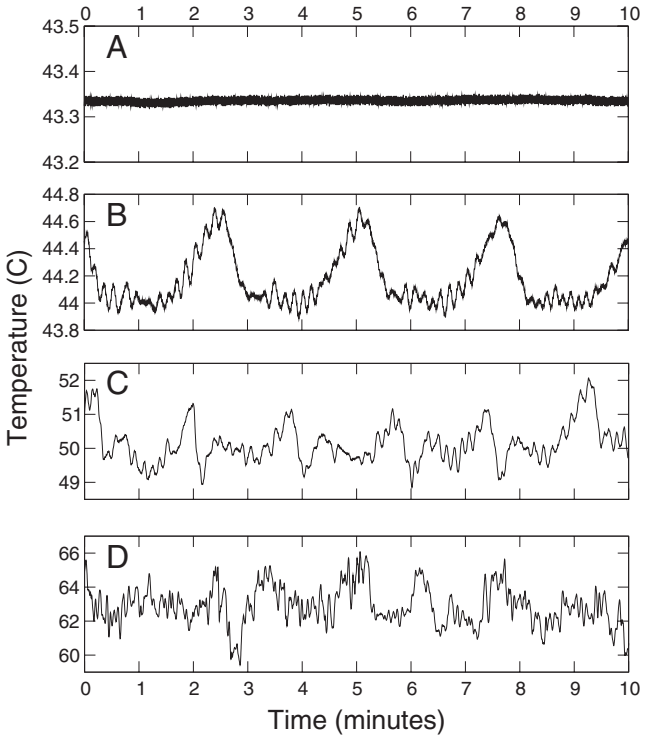

Fig. 4. Temperature time series from within the liquid metal for cases **a**–**d** labeled in Fig. 3. Temperature measurements are made at two-thirds the tank's radius, at midlevel in height, starting from an arbitrary time after thermal equilibrium is reached. All time series are from experiments rotated at 40 revolutions per minute, so that $E = 10^{-6}$. (*A*–*D*) Data are shown (*A*) for $Ra = 1.7 \times 10^7$, (*B*) for $Ra = 3.2 \times 10^7$, (*C*) for $Ra = 5.3 \times 10^7$, and (*D*) for $Ra = 10^8$.

taken at $s = 2h/3$. As the rotating convection experiments grow more supercritical (increasing Ra, E), coherent oscillations are lost to bulk turbulent convection, and convective heat transport becomes more efficient. Fig. 4 *C* and *D* shows temperature time series measurements from the experiments labeled "**c**" and "**d**" in Fig. 3, in which the gradual relative weakening of oscillatory convection can be seen.

Rotationally constrained convection experiences more rapid gains in Nu with increasing Ra than nonrotating convection. However, no clear power law scaling emerges between Nu and Ra in this regime. A stepwise defined $Nu \propto Ra^{\gamma}$ scaling varies smoothly from $\gamma \approx 0.1$ near onset, reaches a maximum value of $\gamma \approx 1.2$, and then appears to asymptote to the nonrotating value of $\gamma = 1/4$ as $Nu \to (1/2)(RaPr)^{1/4}$. In contrast, King et al. (37) report the emergence of a much steeper scaling, $\gamma = 3$, for convection with $Pr \geq 1$ and within a similar range of Ra and E. Alternatively, the ultimate regime for rotationally constrained convection predicts (38) $\gamma = 3/2$, which is closer to the present experimental observations. We stress, though, that we find no clear asymptotic scaling behavior for Nu within the rotationally constrained regime.

Similar to rotating convection in moderate Pr fluids, as Nu is increased to the nonrotating value, there is at first a slight overshoot before the two converge and the influence of rotation is lost. We observe that heat transport by rotating convection surpasses that by nonrotating, but otherwise identical, experiments by up to 6%.

The agreement between heat transfer measurements in nonrotating liquid metal and the inertial scaling [**4**], shown in Fig. 2*B*, suggests that the transition between rotationally constrained and weakly rotating convection should occur when $Ro_c \approx 1$ ([**7**]). Fig. 5 shows heat transfer data for rotating convection normalized by the nonrotating scaling law plotted vs. $Ro_c = \sqrt{(RaE^2/Pr)}$. This regrouping of the parameters effectively collapses the data from Fig. 3 to a single curve. In general, when $Ro_c < 1$, heat transfer is suppressed by the action of the Coriolis force. When $Ro_c > 1$, the data roughly conform to the nonrotating behavior, indicating that rotation is no longer a dominant influence.

Discussion

A summary of results is given in Table 1, in comparison with results from convection with $Pr \geq 1$ (32, 37). In general, we find that convection in liquid metal, with and without rotation, is substantially different from that in moderate Pr fluids. These differences call into question (*i*) the extrapolation of results from models with $Pr = \mathrm{O}(1)$ to liquid metal planetary cores (e.g., ref. 17) and (*ii*) the assumption that turbulence regularizes effective diffusivities such that Pr effects are not important (e.g., ref. 18).

Nonrotating liquid metal convection produces an inertial $Nu \propto Ra^{\gamma}$ scaling with $\gamma = 1/4$ (Fig. 2), rather than the usual $\gamma \approx 1/3$ seen in moderate Pr fluids (32). This difference has been observed previously (e.g., refs. 23, 25, 34, 36). The inertial scaling illustrates the dominant role of interior turbulence in liquid metal convection. In rotating liquid metal convection, we observe no clear Nu–Ra scaling, but rather a sinuous increase of Nu toward the nonrotating regime as Ra is increased beyond its critical value (Fig. 3). In other words, if we assume that $Nu \propto Ra^{\gamma}$, the exponent varies gradually within the range $0.1 \lesssim \gamma \lesssim 1.2$ over Ra-E space. In contrast, similar experiments in moderate Pr fluids transport heat with an exponent as high as $\gamma = 3$ (37). Rapidly rotating liquid metal convection is also complicated by the onset of instability as oscillatory convection. The gradually waning influence of oscillatory convection with increasing supercriticality (Fig. 4) may contribute to the sinuous nature of the Nu–Ra behavior (35). Such effects are not observed in moderate Pr fluids (cf. ref. 49).

In liquid gallium, the transition between the rapidly rotating and weakly rotating convection regimes occurs when $RaE^2/Pr = \mathcal{O}(1)$ (Fig. 5). For similar experiments with $Pr \gtrsim 1$, in contrast, the transition occurs when $RaE^{3/2} = \mathcal{O}(1)$ (37). In planets, where $E < 10^{-10}$, the difference between these two transition scalings is important. The magnetic fields of Jupiter and Saturn (Gas Giants), for example, are generated by convecting metallized hydrogen, with $Pr < 1$ (50). Within Uranus and Neptune (Ice Giants), on

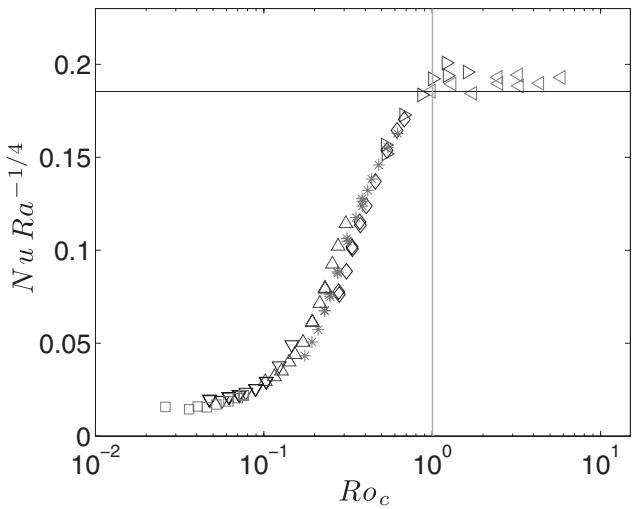

Fig. 5. Reduced Nusselt number, $NuRa^{-1/4}$ is plotted vs. the convective Rossby number, $Ro_c = \sqrt{RaE^2/Pr}$. Symbols indicate Ekman numbers, as in Fig. 3. The solid vertical line shows $Ro_c = 1$. The solid horizontal line indicates the average value for nonrotating convection, $NuRa^{-1/4} = 0.185$.

Table 1. Summary of results from the present study, for which $Pr = 0.025$, in comparison with similar results for $Pr \geq 1$ (32, 37)

Result	$Pr = 0.025$	$Pr \geq 1$
Nonrotating heat transfer	$\gamma = 1/4$	$\gamma = 1/3$
Rotating heat transfer	$\gamma \lesssim 1.2$	$\gamma = 3$
Rotating regime transition	$Ra_t \simeq E^{-2}Pr$	$Ra_t \simeq 10E^{-3/2}$

Heat transfer scaling results are summarized as the exponent γ, for $Nu \propto Ra^{\gamma}$, for both nonrotating $E^{-1} = 0$ and rotationally constrained $Ra < Ra_t$ convection. The transitional Rayleigh number Ra_t defines the partition between rotationally constrained and weakly rotating convection regimes.

the other hand, the magnetic field is most likely generated by the convection of ionic water solution, with $Pr > 1$ (51).

The convective regimes of these planetary dynamos can be estimated using the regime transition criteria [**5**] and [**7**]. To compare the present transition scalings directly with planets, where Ra is poorly constrained, we use instead estimates of flux-Rayleigh numbers, $Rf \equiv Ra \cdot Nu = \alpha g q D^4/(\rho c_P \nu \kappa)$, which depend on the better-constrained planetary heat flux q. Using heat flux measurements from ref. 52 and other estimates from ref. 53, we can estimate that

$$Rf = \left[4 \times 10^{37}; \quad 6 \times 10^{34}; \quad 2 \times 10^{32}; \quad 2 \times 10^{33}\right] \qquad \textbf{[12]}$$

for Jupiter, Saturn, Uranus, and Neptune, respectively.

We can define a transitional flux-Rayleigh number as $Rf_t = Ra_t Nu_t$, where Nu_t is the Nusselt number at which the scaling transitions occur. For $Pr < 1$ (Gas Giants), we have Ra_t from Eq. **7** and, using Eq. **4**, $Nu_t \sim E^{-1/2}Pr^{1/2}$, such that

$$Rf_t \sim E^{-5/2}Pr^{3/2}. \qquad \textbf{[13]}$$

Jupiter and Saturn are estimated to have $E = [10^{-19}; \ 10^{-18}]$ and $Pr = [0.1; \ 0.1]$ (53), such that $Rf_t = [10^{46}; \ 3 \times 10^{43}]$, respectively. Thus, the Gas Giants reside soundly within the rotationally constrained regime, with $Rf \ll Rf_t$.

For $Pr > 1$ (Ice Giants), we have Ra_t from Eq. **5** and, using Eq. **1**, $Nu_t \sim E^{-1/2}$, and therefore

$$Rf_t \sim E^{-2}. \qquad \textbf{[14]}$$

Uranus and Neptune are each estimated to have $E = 10^{-16}$ (53), and therefore $Rf_t = 10^{32}$. The Ice Giants, therefore, are close to the transition between turbulent states, with $Rf = \mathcal{O}(Rf_t)$. Thus, despite the fact that the flux-Rayleigh numbers for the dynamo regions of the Ice Giants are smaller than those of the Gas Giants, the influence of Pr on the nature of the regime transition indicates that convection in Ice Giants may be weakly affected by rotation.

Dynamo action within the Ice Giants produces off-axis, multipolar magnetic fields that differ dramatically from the axial dipoles of the Gas Giants (53). Because little is known of the interiors of these planets, the cause(s) of this division in field morphology is not well understood, and several hypotheses have been put forth, which usually rely on a geometric restriction of the Ice Giant dynamo region (16, 54). Alternatively, dynamo simulations show conclusively that rotationally constrained or weakly rotating convection, respectively, favors either dipolar or multipolar field generation (55). The Ice Giants, however, are colder than the Gas Giants and therefore are not typically thought to be convecting more vigorously. Because the present results suggest that the Gas and Ice Giants may lie in different convection regimes, we put forth the hypothesis here that the difference in field morphologies may be due to the influence of Pr on the transitions between turbulent convection regimes.

ACKNOWLEDGMENTS. Support for laboratory experiment fabrication was provided by the US National Science Foundation (NSF) Instrumentation and Facilities Program. E.M.K. acknowledges the support of the Miller Institute for Basic Research in Science. J.M.A. acknowledges the support of the US NSF Geophysics Program.

1. Chandrasekhar S (1961) *Hydrodynamic and Hydromagnetic Stability* (Clarendon Press, Oxford).
2. Julien K, Legg S, McWilliams J, Werne J (1996) Rapidly rotating turbulent Rayleigh–Bénard convection. *J Fluid Mech* 322:243–273.
3. King EM, Stellmach S, Noir J, Hansen U, Aurnou JM (2009) Boundary layer control of rotating convection systems. *Nature* 457(7227):301–304.
4. Liu Y, Ecke RE (2009) Heat transport measurements in turbulent rotating Rayleigh-Bénard convection. *Phys Rev E Stat Nonlin Soft Matter Phys* 80(3 Pt 2):036314.
5. Stevens RJAM, Zhong JQ, Clercx HJH, Ahlers G, Lohse D (2009) Transitions between turbulent states in rotating Rayleigh-Bénard convection. *Phys Rev Lett* 103(2):024503.
6. Niemela JJ, Babuin S, Sreenivasan KR (2010) Turbulent rotating convection at high Rayleigh and Taylor numbers. *J Fluid Mech* 649:509–522.
7. Schmitz S, Tilgner A (2010) Transitions in turbulent rotating Rayleigh-Benard convection. *Geophys Astrophys Fluid Dyn* 104(5):481–489.
8. Weiss S, Ahlers G (2011) Heat transport by turbulent rotating Rayleigh–Bénard convection and its dependence on the aspect ratio. *J Fluid Mech* 684:407–426.
9. King EM, Aurnou JM (2012) Thermal evidence for Taylor columns in turbulent rotating Rayleigh-Bénard convection. *Phys Rev E Stat Nonlin Soft Matter Phys* 85(1 Pt 2): 016313.
10. Julien K, Rubio AM, Grooms I, Knobloch E (2012) Statistical and physical balances in low Rossby number Rayleigh–Bénard convection. *Geophys Astrophys Fluid Dyn* 106(4–5):392–428.
11. Kunnen RP, Clercx HJ, Geurts BJ (2006) Heat flux intensification by vortical flow localization in rotating convection. *Phys Rev E Stat Nonlin Soft Matter Phys* 74(5 Pt 2): 056306.
12. Zhong JQ, et al. (2009) Prandtl-, Rayleigh-, and Rossby-number dependence of heat transport in turbulent rotating Rayleigh-Bénard convection. *Phys Rev Lett* 102(4): 044502.
13. Weiss S, et al. (2010) Finite-size effects lead to supercritical bifurcations in turbulent rotating Rayleigh-Bénard convection. *Phys Rev Lett* 105(22):224501.
14. Zhong J-Q, Ahlers G (2010) Heat transport and the large-scale circulation in rotating turbulent Rayleigh–Bénard convection. *J Fluid Mech* 665:300–333.
15. Kunnen R, et al. (2011) The role of Stewartson and Ekman layers in turbulent rotating Rayleigh–Bénard convection. *J Fluid Mech* 688:422–442.
16. Jones C (2011) Planetary and stellar magnetic fields and fluid dynamos. *Annu Rev Fluid Mech* 43:583–614.
17. King E, Soderlund K, Christensen UR, Wicht J, Aurnou JM (2010) Convective heat transfer in planetary dynamo models. *Geochem Geophys Geosyst* 11(6):Q06016.
18. Gubbins D (2001) The Rayleigh number for convection in the Earth's core. *Phys Earth Planet Inter* 128(1–4):3–12.
19. Miesch MS (2005) Large-scale dynamics of the convection zone and tachocline. *Living Rev Solar Phys* 2:1.
20. Clever RM, Busse FH (1981) Low-Prandtl-number convection in a layer heated from below. *J Fluid Mech* 102:61–74.
21. Plaut E, Busse FH (2002) Low-Prandtl-number convection in a rotating cylindrical annulus. *J Fluid Mech* 464:345–363.
22. Calkins MA, Aurnou JM, Eldrdge JD, Julien K (2012) The influence of fluid properties on the morphology of core turbulence and the geomagnetic field. *Earth Planet Sci Lett* 359–360:55–60.
23. Cioni S, Ciliberto S, Sommeria J (1997) Strongly turbulent Rayleigh–Bénard convection in mercury: Comparison with results at moderate Prandtl number. *J Fluid Mech* 335: 111–140.
24. Verzicco R, Camussi R (1999) Prandtl number effects in convective turbulence. *J Fluid Mech* 383:55–73.
25. Rossby H (1969) A study of Bénard convection with and without rotation. *J Fluid Mech* 36(2):309–335.
26. Nakagawa Y (1957) Experiments on the instability of a layer of mercury heated from below and subject to the simultaneous action of a magnetic field and rotation. *Proc R Soc Lond A Math Phys Sci* 242(1228):81–88.
27. Aurnou J, Olson P (2001) Experiments on Rayleigh–Bénard convection, magnetoconvection and rotating magnetoconvection in liquid gallium. *J Fluid Mech* 430: 283–307.
28. Aubert J, Brito D, Nataf H, Cardin P (2001) A systematic experimental study of rapidly rotating spherical convection in water and liquid gallium. *Phys Earth Planet Inter* 128(1–4):51–74.
29. Shew WL, Lathrop DP (2005) Liquid sodium model of geophysical core convection. *Phys Earth Planet Inter* 153:136–149.
30. Gillet N, Brito D, Jault D, Nataf H (2007) Experimental and numerical studies of convection in a rapidly rotating spherical shell. *J Fluid Mech* 580:83–121.
31. Aurnou J (2007) Planetary core dynamics and convective heat transfer scaling. *Geophys Astrophys Fluid Dyn* 101(5–6):327–345.
32. Ahlers G, Grossmann S, Lohse D (2009) Heat transfer and large scale dynamics in turbulent Rayleigh-Bénard convection. *Rev Mod Phys* 81:503–537.

33. Malkus WVR (1954) The heat transport and spectrum of thermal turbulence. *Proc R Soc Lond A Math Phys Sci* 225(1161):196–212.
34. Busse FH, Clever RM (1981) An asymptotic model of two-dimensional convection in the limit of low Prandtl number. *J Fluid Mech* 102:75–83.
35. Jones CA, Moore DR, Weiss NO (1976) Axisymmetric convection in a cylinder. *J Fluid Mech* 73(2):353–388.
36. Horanyi S, Krebs L, Muller U (1999) Turbulent Rayleigh-Bénard convection in low Prandtl-number fluids. *Int J Heat Mass Transfer* 42:3983–5003.
37. King EM, Stellmach S, Aurnou JM (2012) Heat transfer by rapidly rotating Rayleigh–Bénard convection. *J Fluid Mech* 691:568–582.
38. Julien K, Knobloch E, Rubio AM, Vasil GM (2012) Heat transport in low-Rossby-number Rayleigh-Bénard convection. *Phys Rev Lett* 109(25):254503.
39. Spiegel EA (1971) Convection in stars. I. Basic Boussinesq convection. *Annu Rev Astron Astrophys* 9:323–352.
40. King EM (2009) An investigation of planetary convection: The role of boundary layers. PhD thesis (Univ of California, Los Angeles).
41. Brandes E, Brook G (1998) *Smithells Light Metals Handbook* (Butterworth-Heinemann, Oxford).
42. Branunsfurth MG, Skeldon AC, Juel A, Mullin T, Riley DS (1997) Free convection in liquid gallium. *J Fluid Mech* 342:295–314.
43. Fukuyama H, Yoshimura T, Yasuda H, Ohta H (2006) Thermal conductivity measurements of liquid mercury and gallium by a transient hot-wire method in a static magnetic field. *Int J Thermophys* 27(6):1760–1788.
44. Touloukian YS, Ho CY (1979) *Thermophysical Properties of Matter*, TPRC Data Series (IFI/Plenum, New York), Vol 14.
45. Davidson PA (2004) *Turbulence* (Oxford University Press, New York).
46. King E, Stellmach S, Buffett B (2012) Scaling behavior in Rayleigh-Bénard convection with and without rotation. J Fluid Mech 717:449–471.
47. Yanagisawa T, et al. (2010) Structure of large-scale flows and their oscillation in the thermal convection of liquid gallium. *Phys Rev E Stat Nonlin Soft Matter Phys* 82(1 Pt 2):016320.
48. Goldstein HF, Knobloch E, Mercader I, Net M (1994) Convection in a rotating cylinder. Part 2. Linear theory for low Prandtl numbers. *J Fluid Mech* 262:293–324.
49. Schmitz S, Tilgner A (2010) Transitions in turbulent rotating Rayleigh-Benard convection. *Geophys Astrophys Fluid Dyn* 104(5–6):481–489.
50. Nellis WJ (2000) Metallization of fluid hydrogen at 140 gpa (1.4 mbar): Implications for Jupiter. *Planet Space Sci* 48:671–677.
51. Lee KKM, et al. (2006) Laser-driven shock experiments on precompressed water: Implications for "icy" giant planets. *J Chem Phys* 125(1):014701.
52. Guillot T (2005) The interiors of giant planets: Models and outstanding questions. *Annu Rev Earth Planet Sci* 33:493–530.
53. Schubert G, Soderlund K (2011) Planetary magnetic fields: Observations and models. *Phys Earth Planet Inter* 187(3–4):92–108.
54. Stanley S, Glatzmaier GA (2010) Dynamo models for planets other than earth. *Space Sci Rev* 152:617–649.
55. Kutzner C, Christensen U (2002) From stable dipolar towards reversing numerical dynamos. *Phys Earth Planet Inter* 131(1):29–45.